J. Fluid Mech. (2007), *vol.* 579, *pp.* 305–314.
doi:10.1017/S0022112007005496 Printed in the United Kingdom

Optimal growth, model reduction and control in a separated boundary-layer flow using global eigenmodes

ESPEN ÅKERVIK[1], JÉRÔME HŒPFFNER[1], UWE EHRENSTEIN[2] AND DAN S. HENNINGSON[1]

[1]Linné Flow Centre, KTH Mechanics, SE-100 44 Stockholm, Sweden
[2]IRPHÉ, Université de Provence, F-13384 Marseille Cedex 13, France

(Received 31 October 2006 and in revised form 13 February 2007)

Two-dimensional global eigenmodes are used as a projection basis both for analysing the dynamics and building a reduced model for control in a prototype separated boundary-layer flow. In the present configuration, a high-aspect-ratio smooth cavity-like geometry confines the separation bubble. Optimal growth analysis using the reduced basis shows that the sum of the highly non-normal global eigenmodes is able to describe a localized disturbance. Subject to this worst-case initial condition, a large transient growth associated with the development of a wavepacket along the shear layer followed by a global cycle related to the two unstable global eigenmodes is found. The flow simulation procedure is coupled to a measurement feedback controller, which senses the wall shear stress at the downstream lip of the cavity and actuates at the upstream lip. A reduced model for the control optimization is obtained by a projection on the least stable global eigenmodes, and the resulting linear-quadratic-Gaussian controller is applied to the Navier–Stokes time integration. It is shown that the controller is able to damp out the global oscillations.

1. Introduction

Open flows, such as boundary layers, wakes and mixing layers, are subject to convective instabilities, where the flow acts as an amplifier of disturbances as they are transported downstream. For some of the flow cases and in particular parameter ranges self-sustained oscillations may occur. This self-sustaining mechanism can be captured by the unstable global eigenmodes of the linearized Navier–Stokes operator. However, a combination of damped global modes is also capable of representing convective instabilities in non-parallel flows (Cossu & Chomaz 1997; Schmid & Henningson 2002; Ehrenstein & Gallaire 2005). Numerical investigations performed by Marquillie & Ehrenstein (2003) addressed separated boundary-layer flow produced by two-dimensional bump geometries. They showed that elongated separation bubbles are likely to undergo bursting leading to unsteadiness. By confining the recirculation bubble between two successive bumps on the plate, Marquillie & Ehrenstein (2003) interpreted the flow oscillations in terms of the existence of a global saturated mode oscillating with a well-defined period. Building on their findings we introduce a smooth high-aspect-ratio (length to depth ratio $L/D \approx 25$) cavity-like geometry, which induces a geometrically confined separation bubble in the boundary-layer flow as shown in figure 1. Note that this flow case differs from the sharp-edged small-aspect-ratio (typically $L/D = 2$) high-Reynolds-number compressible cavity flow arising in

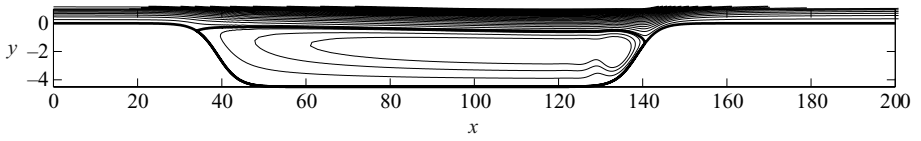

FIGURE 1. Streamlines of the steady-state base flow solution used for stability analysis at $Re = 350$. The thick line represents the zero level contour. Note the large aspect ratio of $L/D \approx 25$ and the smooth lips.

aerospace applications (see e.g. Rowley & Williams 2006). We view this flow case as a prototype separated flow, where both streamwise non-normality and global instability play a central role. In this non-parallel configuration global eigenmodes of the linearized Navier–Stokes operator become a natural tool for stability analysis. Here we first show that a sum of the non-normal global modes describes well the development of a wavepacket and the onset of a global oscillating cycle associated with the two unstable eigenmodes. Given this ability to reproduce the flow dynamics, the eigenmodes are used as a basis for a Petrov/Galerkin projection, enabling us to build a reduced-order model for control.

During the last decade modern control theory has increasingly been applied to fluid flow problems, given the available computer capacities and sensor/actuator developments. Linear optimal control theory has been introduced for flow systems governed by linear instability mechanisms (Bewley & Liu 1998), such as for instance spatially developing boundary layers (Högberg & Henningson 2002) and it may also be relevant for nonlinear flows, such as turbulent boundary layers (Kim 2003). Optimal control of fluid flow based on a full state-space representation of the flow field necessitates manipulation of very high-dimensional dynamical systems. In weakly non-parallel flow configurations the problem may become tractable by determining control and estimation kernels for individual wavenumbers in the approximately homogeneous space directions (Högberg & Henningson 2002). In practical flow situations full state information is not available, hence the flow state must be estimated based on sensor measurements. The estimation process can be seen as an optimal filtering problem using a Kalman filter, based on the linearized Navier–Stokes equations. Appropriate stochastic models for the relevant statistics of sensor noise and external disturbances are essential in order to extract the relevant information from the system (Hœpffner *et al.* 2005). In the present work we use the linear quadratic Gaussian (LQG) control synthesis, where the two subproblems of full information control and estimation are solved separately in an optimal manner. Combining the two leads to an optimal measurement feedback control, where the estimated flow is used for control feedback (see e.g. Lewis & Syrmos 1995).

The design of the controller is intimately related to model reduction and the usual procedure is that of projecting the equations onto a subspace. One possible approach is to use the proper orthogonal decomposition modes of the excited flow, thereby capturing the high-energy content of the flow. Balanced truncation provides a more attractive basis by selecting vectors that are equally controllable and observable. When the system becomes large (e.g. 1000 states or more) the standard approach of directly solving Lyapunov equations needed for balanced truncation becomes intractable. Rowley (2005) discussed a computationally tractable approach to obtaining the balancing vectors, based on time-marching algorithms. In globally unstable flow configurations, the global eigenmodes of the linearized Navier–Stokes system form a natural projection basis due to their immediate physical interpretation. For instance

one can judge the best placement of the sensors and actuators for observability and controllability, intimately connected to the localization of the least stable direct and adjoint modes respectively (Chomaz 2005).

2. Flow configuration and numerical methods

The Navier–Stokes equations are solved in the domain $0 \leqslant x \leqslant 400$, $\eta(x) \leqslant y < 80$, large enough to recover free-stream uniform flow. All variables are made non-dimensional with the displacement thickness δ^* and the free-stream velocity U_∞ at the inflow $x = 0$, where a Blasius profile is prescribed. The Reynolds number is defined as $Re = U_\infty \delta^*/\nu$, where ν is the kinematic viscosity. The function $\eta(x)$ is the graph of the wall. The smooth cavity is symmetric with respect to its centre at $x_c = 89$, and its upstream part is given by $\eta(x) = -2.25(\tanh(a(x-b))+1)$, $0 \leqslant x \leqslant x_c$ with $a = 0.2$ and $b = 39$ matching smoothly the flat plate upstream and downstream.

The streamlines in a subset of the computational domain for the steady state at $Re = 350$ are depicted in figure 1. Note that the main effect of the smooth cavity is the generation of a recirculation zone and a shear layer. The direct numerical simulation (DNS) procedure has been used in Marquillie & Ehrenstein (2003). Accounting for wall curvature, a mapping transforms the physical coordinates into the computational ones, which are discretized using fourth-order finite differences in the streamwise direction (with 2048 grid points) and Chebyshev-collocation in the vertical direction (with 97 collocation points).

2.1. *Steady state*

We found that above $Re = 325$ the flow became subject to self-sustained oscillations. For a general geometry of this type it is the Reynolds number combined with the length to depth ratio L/D and the non-dimensional depth D/δ^* that constitute the relevant non-dimensional quantities; however when fixing the length and depth of the smooth cavity the Reynolds number is the only relevant bifurcation parameter. In a globally unstable regime any noise present in the high-order numerical discretization will grow exponentially, making it impossible to numerically compute a steady-state solution by standard time-marching methods. Therefore the technique proposed in Åkervik *et al.* (2006) is used to recover the steady state at the current Reynolds number of $Re = 350$. The Navier–Stokes equations are forced by adding a term proportional to the difference between the flow state and a filtered solution. If $\dot{q} = \mathrm{NS}(q)$ represents the nonlinear Navier–Stokes system, the modified system is

$$\dot{q} = \mathrm{NS}(q) - \chi(q - \bar{q}), \quad \dot{\bar{q}} = (q - \bar{q})/\Delta, \tag{2.1}$$

where the right-hand equation represents the differential form of a causal low-pass temporal filter. The steady state of (2.1) is also a steady state of the Navier–Stokes system. A filter width of $\Delta = 15$ has been chosen such that the frequencies of the instability are targeted and a damping coefficient $\chi = 0.02$ was found to be appropriate (see Åkervik *et al.* 2006).

2.2. *Eigenmodes*

The global eigenmodes are computed by linearizing the Navier–Stokes system about the steady state $\boldsymbol{U}(x, y) = (U(x, y), V(x, y))$. The disturbance flow field $\boldsymbol{u}(x, y, t) = \hat{\boldsymbol{u}}(x, y)\,\mathrm{e}^{-\mathrm{i}\omega t}$ and pressure $p(x, y, t) = \hat{p}(x, y)\,\mathrm{e}^{-\mathrm{i}\omega t}$ satisfy the partial differential system

$$-\mathrm{i}\omega\hat{\boldsymbol{u}} = -(\boldsymbol{U}\cdot\nabla)\hat{\boldsymbol{u}} - (\hat{\boldsymbol{u}}\cdot\nabla)\boldsymbol{U} - \nabla\hat{p} + \frac{1}{Re}\nabla^2\hat{\boldsymbol{u}}, \tag{2.2}$$

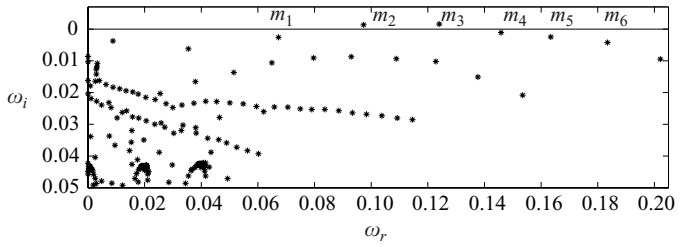

FIGURE 2. Eigenvalues of the direct problem (2.4). There are two unstable modes. The modes labelled $m_1 - m_6$ are depicted in figure 3.

$$0 = \nabla \cdot \hat{\boldsymbol{u}}. \tag{2.3}$$

After discretization this is written

$$-\mathrm{i}\omega_l \boldsymbol{B}\boldsymbol{q}_l = \boldsymbol{A}\boldsymbol{q}_l \quad \text{with adjoint} \quad \mathrm{i}\omega_l \boldsymbol{B}^H \boldsymbol{q}_l^+ = \boldsymbol{A}^H \boldsymbol{q}_l^+ \tag{2.4}$$

for the eigenfunction $\boldsymbol{q}_l$ with corresponding adjoint eigenfunction $\boldsymbol{q}_l^+$, $\boldsymbol{B}$ is the projection of the total disturbance field on the velocity components; $\boldsymbol{A}^H$ is the adjoint discretized operator (conjugate transpose), and the bi-orthogonality condition $\langle \boldsymbol{q}_k, \boldsymbol{B}\boldsymbol{q}_l^+ \rangle = \delta_{kl}$ with respect to the finite-dimensional inner product applies. The operators of the eigenvalue problem have been discretized on a domain of extent $0 \leqslant x \leqslant 300$, $\eta(x) \leqslant y \leqslant 75$, sufficiently large to produce converged eigenmodes. Homogeneous Dirichlet boundary conditions are used at all boundaries except at the outflow, where a homogeneous Neumann condition is imposed. The domain is mapped into $[-1, 1] \times [-1, 1]$ and a Chebyshev-Chebyshev collocation discretization is used. The basic steady flow is then interpolated on the new grid. A similar procedure has been used in Ehrenstein & Gallaire (2005) for the computation of global modes in the flat-plate boundary layer. A collocation grid with 350×65 collocation points yielded converged stability results. The resulting eigenvalue problem is far too large to be solved by standard QZ algorithms. However Krylov subspace projections with dimension $m = 800$ together with the Arnoldi algorithm (see Nayar & Ortega 1993) proved suitable to recover the part of the spectrum relevant for our analysis. For the steady state shown in figure 1 the spectrum is depicted in figure 2. For the present parameters there are two unstable eigenvalues labelled m_2 and m_3 (only half of the spectrum with $\omega_r > 0$ is shown). Figure 3(a–f) shows the vertical velocity components of the direct eigenfunctions associated with the eigenvalues labelled m_1–m_6 in figure 2, respectively. As can be seen, there are many similar eigenfunctions, a typical feature of non-normal operators, and in the following section we will describe the implications of this for optimal growth. The vertical velocity component of the adjoint eigenfunction corresponding to the least stable eigenvalue m_3 is depicted in figure 3(g). We observe a clear separation in space between the direct (see figure 3c) and adjoint eigenfunctions, indicating a strong streamwise non-normality (see Chomaz 2005).

3. Optimal growth

For sufficiently low-amplitude flow perturbations $\boldsymbol{q}(t)$, an eigenmode expansion

$$\boldsymbol{q}(t) = \sum_{l=1}^{N} \kappa_l(t) \boldsymbol{q}_l \tag{3.1}$$

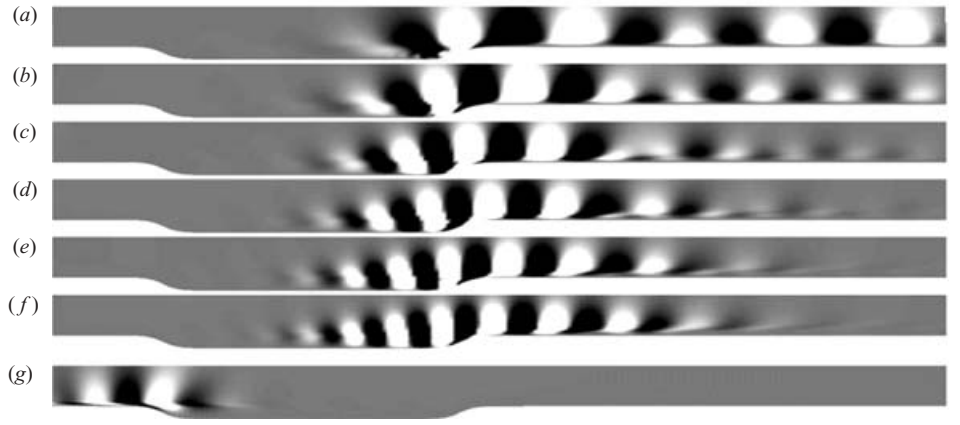

FIGURE 3. (a–f) Vertical velocity components of direct eigenfunctions corresponding to the eigenvalues labelled $m_1 - m_6$ in figure 2, respectively. (g) Adjoint eigenfunction corresponding to m_3, the most unstable eigenvalue. Black indicates large negative values and white indicates large positive values, with the grey tones between. The domain is truncated at $y = 14$.

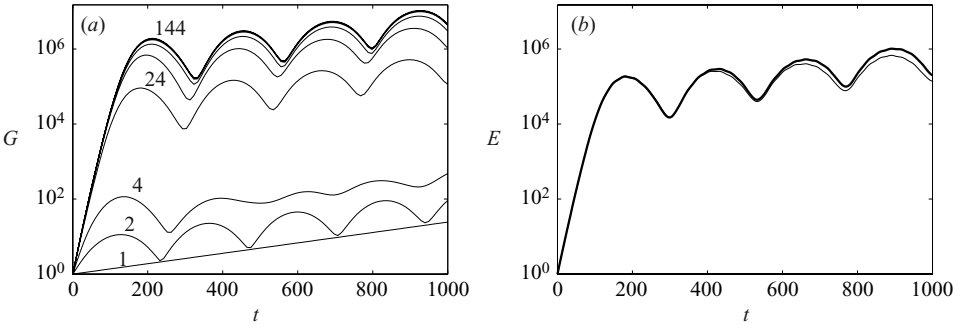

FIGURE 4. (a) Envelope of maximum energy growth from initial conditions. The different lines correspond to an increasing number of eigenmodes included in the optimization, $1, 2, 4, 24, \ldots, 124, 144$ from bottom to top. (b) One realization using initial condition based on 100 modes: thick line shows the eigenmode system integrated in time and the thin line shows DNS evolution.

can be used to describe the flow dynamics. The flow evolution is initiated by superimposing the optimal initial condition $\boldsymbol{q}_0$ on the steady state, leading to the maximum energy growth $\|\boldsymbol{q}(t)\|_E$ at a given time t:

$$G(t) = \max_{\boldsymbol{q}_0 \neq 0} \frac{\|\boldsymbol{q}(t)\|_E}{\|\boldsymbol{q}_0\|_E}. \tag{3.2}$$

The procedure to compute the optimal initial condition is outlined in Schmid & Henningson (2001) and the subsequent energy envelope for the present flow case is depicted in figure 4(a). Using one mode we observe the exponential growth of the most unstable mode. All of the direct eigenfunctions shown in figure 3 are similar; they are oscillatory and exponentially growing along the shear layer. By optimally summing the non-normal eigenmodes, cancellation results in an upstream-located initial wavepacket. This leads to a fast transient energy growth up to $t = 200$, followed by a global cycle with a period of approximately 300 time units. This cycle is associated with the least stable eigenvalues in figure 2. Since the real parts of these modes are a

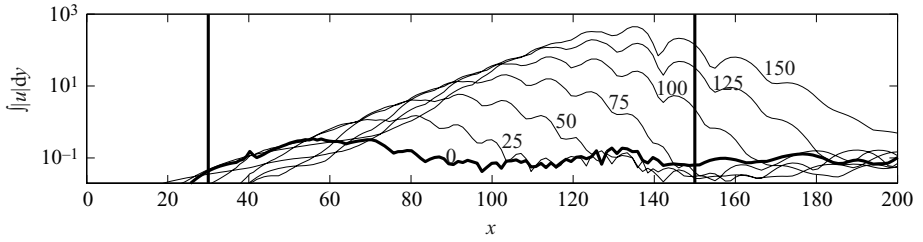

FIGURE 5. Snapshots of the y-integrated streamwise velocity at times $0, 25, \ldots, 150$, showing the propagation of a wavepacket in the eigenmode system. The thick line shows the initial disturbance. The vertical lines indicates the approximate start and end of the recirculation region.

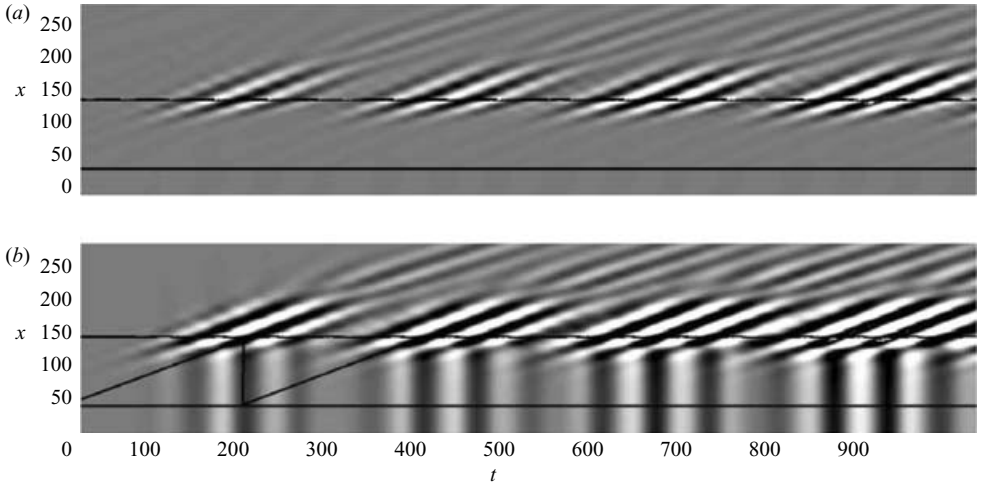

FIGURE 6. x/t diagram for (a) the vertical flow velocity at $y = 2$ and (b) the pressure at $y = 10$, tracing the quantities in the streamwise direction and in time at their respective vertical position. Black indicates large negative values whereas white indicates large positive values. The flow initial condition is the optimal initial condition. The horizontal lines show the location of the cavity lips. The oblique lines trace the path of the wavepacket back to its origin and the triggering position at the upstream lip of the cavity at the first reflection.

distance of $\delta \approx 0.02$ apart, and the corresponding eigenfunctions have a very similar structure, they have the ability to cancel each other, giving rise to a 'beating' with a period of $2\pi/\delta$. Schmid & Henningson (2002) observed the same phenomena when studying a model equation for a falling liquid curtain. Figure 4(b) shows the actual energy evolution when integrating the eigenmode system (thick line) and DNS system (thin line) in time using the optimal initial condition based on 100 modes, confirming the ability of the eigenmode system to describe the relevant flow dynamics. Note that in the DNS system the initial condition is superimposed on the steady state.

The initial evolution of the wavepacket in the eigenmode system is shown in figure 5. We observe the spatial exponential growth in disturbance amplitude as the wavepacket propagates along the shear layer. The spatio-temporal diagram of the dynamics in the DNS system is depicted in figure 6, where one sees the convection and growth of the wavepacket along the shear layer, and regeneration at the upstream cavity lip. A global pressure change, visible in the form of vertical rays, occurs when

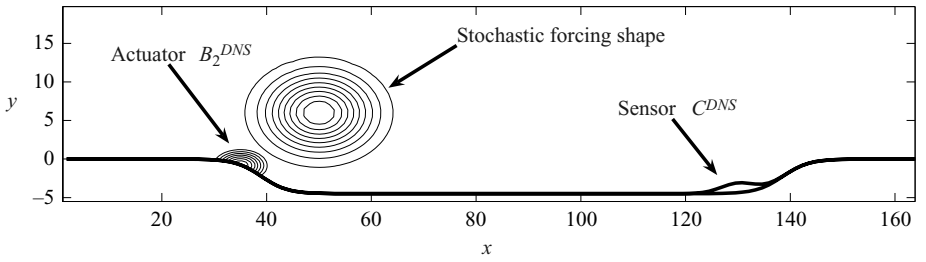

FIGURE 7. Sketch of the control setting, with a volume forcing actuator, and a wall skin friction sensor.

the wavepacket reaches the downstream cavity lip; the subsequent propagation of the regenerated wavepacket is highlighted by the oblique line. This instability mechanism may be seen as a destabilization of the global mode by the pressure field, where the pressure yields an immediate feedback mechanism and the strong streamwise non-normality causes a large growth of the disturbances along the shear layer.

4. Control

To control the cavity flow, we introduce one sensor and one actuator as sketched in figure 7. The actuator is located at the upstream limit of the cavity, where the least stable adjoint eigenfunctions have their maximum, so as to trigger the most efficient response. The least stable adjoint eigenfunction is shown in figure 3(*c*). The sensor is placed in the vicinity of the downstream cavity lip where the eigenfunctions have large amplitude. The sensor measures the wall shear stress $\int \mathscr{C}(x)(\partial u/\partial y)\,\mathrm{d}x$, where $\mathscr{C}(x)$ is a Gaussian function with a width of ≈ 20. This operation may formally be written as $r = C^{DNS} q$ for the flow state q. The actuator is a volume forcing of Gaussian shape on the vertical velocity component located close to the wall at the upstream cavity lip, with a width of ≈ 20 and a height of ≈ 2.

A dynamic model for the cavity flow is constructed using the eigenmode expansion (3.1). Based on this model an LQG control procedure gives rise to the system

$$\left.\begin{aligned} \dot{\boldsymbol{k}} &= \boldsymbol{A}\boldsymbol{k} + \boldsymbol{B}_1 w + \boldsymbol{B}_2 \phi, & r &= \boldsymbol{C}\boldsymbol{k} + g, \\ \dot{\boldsymbol{k}}_e &= \boldsymbol{A}\boldsymbol{k}_e + \boldsymbol{B}_2 \phi - \boldsymbol{L}(r - r_e), & r_e &= \boldsymbol{C}\boldsymbol{k}_e, \\ \phi &= \boldsymbol{K}\boldsymbol{k}_e. \end{aligned}\right\} \tag{4.1}$$

The vector $\boldsymbol{k}(t) = [\kappa_1(t), \ldots, \kappa_N(t)]^T$ of the expansion coefficients of the flow obeys the model dynamics, where $\boldsymbol{A}$ is now the diagonal matrix of the eigenvalues. The external disturbances are modelled as white noise stochastic input $w(t)$ with variance W, and $\boldsymbol{B}_1$ is the projection on the eigenmodes of the Gaussian-shaped spatial forcing function centred at $x = 50$. The projected actuator is denoted $\boldsymbol{B}_2$, and $\phi(t)$ is the actuation signal. These projections are achieved by performing the inner product with the adjoint modes. The measurement is denoted r, and $\boldsymbol{C}$ is the measurement matrix. The measurement is corrupted by a stochastic sensor noise $g(t)$ with variance G^2. An estimator is constructed, with estimated state $\boldsymbol{k}_e$, obeying the model dynamics, and with an estimation feedback forcing $\boldsymbol{L}(r - r_e)$. The estimation gain $\boldsymbol{L}$ will be designed such that the estimated state $\boldsymbol{k}_e$ converges to the flow state $\boldsymbol{k}$, i.e. minimizes the mean kinetic energy of the estimation error $\boldsymbol{k} - \boldsymbol{k}_e$. The control actuation ϕ is a feedback of the estimated flow state, with control feedback gain $\boldsymbol{K}$ that will be designed such as to minimize a weighted sum of the flow mean kinetic energy and the actuation effort.

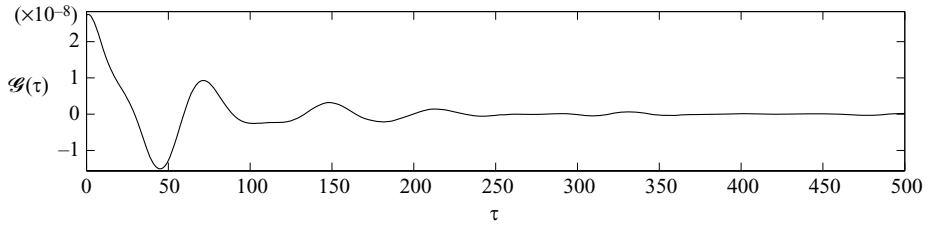

FIGURE 8. Impulse response $\mathscr{G}(\tau)$ from measurement signal to control signal. The controller uses information from about 350 time units in the past.

A central issue is the controllability and observability of the flow for the chosen actuator and sensor pair. Since, as observed in § 3, the eigenmodes capture the relevant dynamics, the magnitude of the projections $\boldsymbol{B}_2$ and $\boldsymbol{C}$ of the actuator and sensor indicate the controllability and observability for each eigenmode. In this manner one can choose the shape and location of the actuator and sensor based on the magnitude of these coefficients on the relevant modes as a measure of the quality of the representation of the actuator and sensor in the reduced system. We have checked that the response from an impulsive input from the actuator in the DNS and in the eigenmode system give the same measurement signal in the two systems.

The optimal feedback gains $\boldsymbol{K}$ and $\boldsymbol{L}$ that minimize the flow and estimation error mean kinetic energy are found by the solution of two algebraic Riccati equations (see Skelton 1988)

$$0 = \boldsymbol{A}^H\boldsymbol{X}_c + \boldsymbol{X}_c\boldsymbol{A} - \boldsymbol{X}_c\boldsymbol{B}_2\ell^{-2}\boldsymbol{B}_2^H\boldsymbol{X}_c + \boldsymbol{Q},$$
$$0 = \boldsymbol{A}\boldsymbol{X}_e + \boldsymbol{X}_e\boldsymbol{A}^H - \boldsymbol{X}_e\boldsymbol{C}^H G^{-2}\boldsymbol{C}\boldsymbol{X}_e + \boldsymbol{B}_1 W\boldsymbol{B}_1^H,$$

for the matrix unknowns $\boldsymbol{X}_c$ and $\boldsymbol{X}_e$, and the feedback gains can be obtained as $\boldsymbol{K} = -\ell^{-2}\boldsymbol{B}_2\boldsymbol{X}_c$ and $\boldsymbol{L} = -\boldsymbol{X}_e\boldsymbol{C}^H G^{-2}$. In our computations, we have assumed an external disturbance w with unit variance ($W = 1$). The control penalization and sensor noise variance were chosen as $\ell = 5\times10^5$ and $G = 7\times10^5$ in order to enforce low-amplitude feedback gains. The matrix $\boldsymbol{Q}$ is defined such that $\boldsymbol{k}^H\boldsymbol{Q}\boldsymbol{k}$ measures the kinetic energy of the disturbances.

Once the two Riccati equations are solved and the feedback gains are obtained, we can couple the flow and the controller in the following manner:

$$\dot{q} = \mathrm{NS}(q) + B_2^{DNS}\phi, \qquad r = C^{DNS}q, \tag{4.2}$$
$$\dot{\boldsymbol{k}}_e = (\boldsymbol{A} + \boldsymbol{B}_2\boldsymbol{K} + \boldsymbol{L}\boldsymbol{C})\boldsymbol{k}_e - \boldsymbol{L}r, \qquad \phi = \boldsymbol{K}\boldsymbol{k}_e, \tag{4.3}$$

where B_2^{DNS} and C^{DNS} are the actuator and sensor expressed in the DNS. The measurement r is driving the estimated state $\boldsymbol{k}_e$, which in turn is updated online by a Crank–Nicholson time-integration procedure, feeding back the control signal ϕ to the DNS at every time step.

To emphasize the linear relation between the measurement signal and the control signal through the controller system, we can write

$$\phi(t) = \int_0^\infty \underbrace{\boldsymbol{K}\,\mathrm{e}^{(\boldsymbol{A}+\boldsymbol{B}_2\boldsymbol{K}+\boldsymbol{L}\boldsymbol{C})\tau}\boldsymbol{L}}_{\mathscr{G}(\tau)}\, r(t-\tau)\,\mathrm{d}\tau, \quad r(t) = 0, t < 0, \tag{4.4}$$

where $\mathscr{G}(\tau)$ is the impulse response from r to ϕ, and illustrates how the actuation $\phi(t)$ depends on past measurements $r(t-\tau)$. The impulse response is shown in figure 8. Note that this formulation could provide an alternative hardware implementation

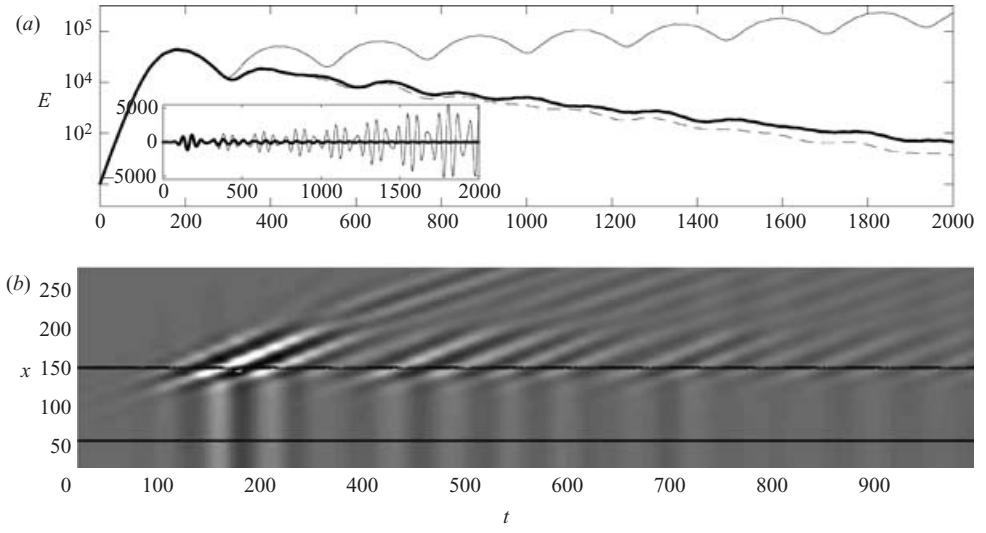

FIGURE 9. (*a*) Energy of the uncontrolled flow (thin solid line), controlled flow using the model with four modes (thick solid) and 25 modes (dashed). Inset shows the sensor signal in the uncontrolled case as thin solid line and controlled using four modes as thick solid line. (*b*) x/t diagram for the pressure when the control is applied. This is to be compared to figure 6(*b*).

of the controller. In order to assess the performance of the computed control and estimation gains the controller is applied to the same configuration that led to the evolution shown in figure 6. Reduced models consisting of the 25 and the four least stable eigenmodes are considered. Figure 9(*a*) shows that when control is applied, the exponential energy growth is turned into an exponential decay after the first peak. There is an almost equivalent performance for both controller dimensions. The sensor signals for the controlled and uncontrolled case are shown in the inset in figure 9(*a*). The sensor signal from the controlled case decays after the first reflections of the wavepacket at $t \approx 125$. It is not possible to control the initial energy growth, before the wavepacket has reached the sensor located at the downstream cavity lip. The x/t diagram for the controlled flow in figure 9(*b*) is to be compared with figure 6(*b*). When the control is applied one still sees the vertical rays of the global pressure changes but the wavepacket regeneration is reduced, leading to a decrease in the levels of fluctuations at each cycle, i.e. flow stabilization.

5. Conclusions

The cavity flow considered here may be seen as a prototype of non-parallel flow with self-sustained global instability behaviour. Owing to the non-normallity of the underlying operator, computed eigenmodes are sensitive to numerical errors and require high resolution even when using spectral collocation. This sensitivity is, however, mostly seen in loss of accuracy for the location of eigenvalues in the complex plane; the mechanism of wavepacket propagation followed by pressure reflections obtained through optimally summing the non-normal modes proved robust and in close agreement with DNS, even at lower resolution. Despite the fact that about 100 modes are required for converged results of optimal growth, many fewer modes are needed for a stabilizing controller. There is only a negligible loss of control performance when using as few as four modes in the reduced model. The small

controller is run in parallel with the DNS at a low computational cost, and provides the feedback control signal based on the measurement signal taken from the full DNS. The satisfactory performance of the controller, combined with the low online computational effort, means that the use of reduced-order models for fluid flows, built by projection on global eigenmodes in the LQG framework, has promise for the future.

REFERENCES

Åkervik, E., Brandt, L., Henningson, D. S., Hœpffner, J., Marxen, O. & Schlatter, P. 2006 Steady solutions of the Navier–Stokes equations by selective frequency damping. *Phys. Fluids* **18**, 068102.

Bewley, T. R. & Liu, S. 1998 Optimal and robust control and estimation of linear paths to transition. *J. Fluid Mech.* **365**, 305–349.

Chomaz, J. M. 2005 Global instabilities in spatially developing flows: non-normality and nonlinearity. *Annu. Rev. Fluid Mech.* **37**, 357–392.

Cossu, C. & Chomaz, J. 1997 Global measures of local convective instability. *Phys. Rev. Lett.* **77**, 4387–90.

Ehrenstein, U. & Gallaire, F. 2005 On two-dimensional temporal modes in spatially evolving open flows: the flat-plate boundary layer. *J. Fluid Mech.* **536**, 209–218.

Hœpffner, J., Chevalier, M., Bewley, T. R. & Henningson, D. S. 2005 State estimation in wall-bounded flow systems. Part 1. Laminar flows. *J. Fluid Mech.* **543**, 263–294.

Högberg, M. & Henningson, D. S. 2002 Linear optimal control applied to instabilities in spatially developing boundary layers. *J. Fluid Mech.* **470**, 151–179.

Kim, J. 2003 Control of turbulent boundary layers. *Phys. Fluids* **15**, 1093–1105.

Lewis, F. & Syrmos, V. 1995 *Optimal control*. John Wiley and Sons.

Marquillie, M. & Ehrenstein, U. 2003 On the onset of nonlinear oscillations in a separating boundary-layer flow. *J. Fluid Mech.* **490**, 169–188.

Nayar, M. & Ortega, U. 1993 Computation of selected eigenvalues of generalized eigenvalue problems. *J. Comput. Phys.* **108**, 8–14.

Rowley, C. R. 2005 Model reduction for fluids, using balanced proper orthogonal decomposition. *Intl J. Bifurcation Chaos* **15**, 997–1013.

Rowley, C. R. & Williams, D. R. 2006 Dynamics and control of high-reynolds-number flow over open cavities. *Annu. Rev. Fluid Mech.* **38**, 251–276.

Schmid, P. J. & Henningson, D. S. 2001 *Stability and Transition in Shear Flows*. Springer.

Schmid, P. J. & Henningson, D. S. 2002 On the stability of a falling liquid curtain. *J. Fluid Mech.* **463**, 163–171.

Skelton, R. E. 1988 *Dynamics System Control*. John Wiley and Sons.